

Predicting the fire performance of LSF walls made of web stiffened channel sections

Yomal Dias*, Poologanathan Keerthan, Mahen Mahendran

Queensland University of Technology (QUT), Brisbane, Australia

ARTICLE INFO

Keywords:

Light gauge steel framed walls
Web stiffened channel sections
Finite element analyses
Fire resistance level

ABSTRACT

Fire performance of plasterboard lined Light-gauge Steel Framed (LSF) walls has been investigated using numerical and experimental studies in the past. However, past research has been limited to lipped channel sections (LCS) and welded hollow flange channel (HFC) sections. This paper investigates the fire performance of LSF walls made of a new web-Stiffened Channel Section (SCS) stud using numerical models, validated using available fire test results. The SCS succeeds in eliminating both local and distortional buckling when used as 3 m long LSF wall studs at ambient temperature. Ambient temperature compression capacity evaluations showed that the performance of the SCS is equivalent to the welded HFC, but is superior to the LCS. Fire performance of load bearing and non-load bearing LSF walls made with each of the three stud sections was assessed for three common wall configurations using thermal and structural finite element analyses. Extended FRL versus Load Ratio curves were developed using a combination of steady state and transient state coupled temperature-displacement analyses. The results showed that the effect of stud geometry on the fire performance of LSF wall configurations is minimal. Under the same load ratio, all three stud sections perform similarly in each of the wall configurations. Considering the ambient and fire performance results, the reduced cost and also the potential double connectivity to plasterboard via its lip elements, the SCS is recommended for use in LSF walls. This paper has also highlighted the susceptibility of non-load bearing LSF walls to fail in fire under structural inadequacy.

1. Introduction

Light Gauge Steel Frame (LSF) wall systems are increasingly being used in low to mid-rise constructions across the world due to their lightweight, ease of fabrication and erection, high-quality finish, and low wastage [1]. Although predominantly used as non-load bearing drywall panels, these wall systems can also be designed to act as primary load bearing members providing strength and stability in multi-storey buildings. The basic components of an LSF wall are shown in Fig. 1(a). A typical wall consists of a cold-formed steel frame made of studs and tracks sheathed on both sides with gypsum plasterboards using self-drilling screws. Conventionally, mono-symmetric un-lipped and lipped channel sections (LCS) have been used to form the primary load bearing studs in such walls. Fire performance of such LSF wall systems has been assessed through a series of experiments [2–5]. More recently, the possibility of using welded hollow flange channel (HFC) sections, commonly known as the LiteSteel Beam (LSB), as LSF wall studs was also assessed [6]. However, these attempts have failed to produce a significant enhancement in the Fire Resistance Level (FRL) of LSF walls. The LCS and welded HFC are shown in Fig. 1, along with a

rivet-fastened HFC section. Rivet fastening is considered to be an economical substitute to welding. Fire performance of LSF walls made with rivet-fastened HFC sections is yet to be assessed. Regardless, the prospects of a successful outcome are low as the ultimate compression capacity of rivet fastened HFC sections was found to be as much as 40% lower than that of an equivalent welded section [7].

Web stiffening options are extensively being used in modern cold-formed steel (CFS) sections to enhance their performance by eliminating local buckling. Additionally, they facilitate the integration of a greater amount of steel without changing the overall stud cross-section dimensions. The fire performance of unstiffened and web-stiffened single and built-up CFS beams has been studied before [8,9]. However, the elevated temperature performance of axially loaded web-stiffened channel sections, specifically addressing LSF wall applications, is yet to be investigated in detail.

Numerical modelling provides an efficient alternative to time consuming and costly full-scale testing of LSF walls. Extensive research has been done to simulate full-scale fire tests of LSF walls, especially using the commercially available Finite Element (FE) analysis software ABAQUS in the past. Feng and Wang [4] developed numerical models

* Corresponding author.

E-mail addresses: yomal.dias@hdr.qut.edu.au (Y. Dias), keeds123@qut.edu.au (P. Keerthan), m.mahendran@qut.edu.au (M. Mahendran).

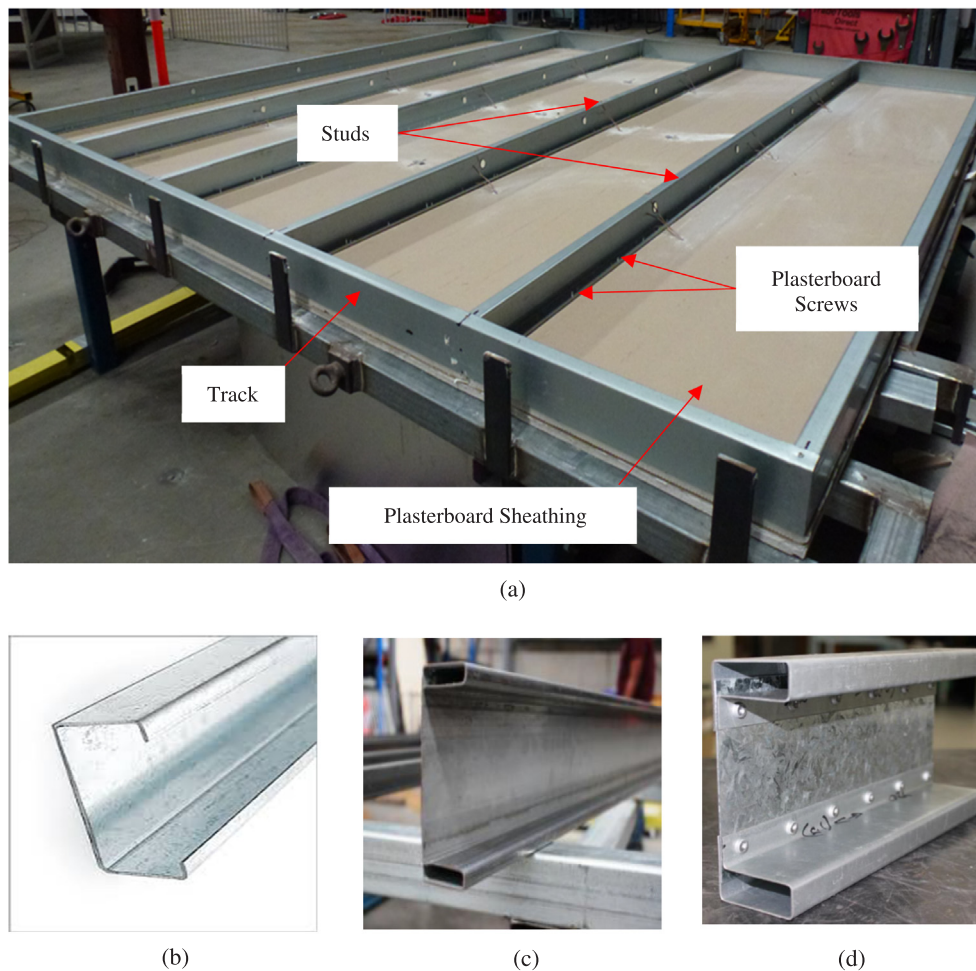


Fig. 1. LSF wall panel and studs (a) Wall components (b) Lipped channel, (c) Welded HFC, (d) Riveted HFC.

using ABAQUS to determine the axial compression strength of lipped channel sections subjected to non-uniform temperature fields across the stud. Their conclusions state that the non-uniform temperature field of a stud subjected to fire can be simplified with uniform temperatures in the flanges and lips, and a linear temperature variation across the web. Further improvements to this method have been done subsequently [9–11]. Gunalan and Mahendran [12], through their validated FE structural models of full-scale load bearing fire tests, established the critical stud hot flange (HF) temperatures and stated that the limiting temperature of 350 °C in EN 1993-1-2 [13] is too conservative. Fire performance of load bearing LSF walls with LSB studs was numerically simulated by Kesawan and Mahendran [14].

This paper primarily investigates the structural fire performance of the web-Stiffened Channel Section (SCS) shown in Fig. 2(c) when used as a load bearing stud section in LSF walls in compression and compares it against the two other sections shown in Fig. 2(a) and (b). The additional 12 mm lip of the SCS is intended to provide double connectivity to the plasterboard. All three sections were considered to be made of the same grade steel with a nominal yield strength of 300 MPa. The ambient temperature buckling and ultimate capacities were evaluated using both Finite Strip and Finite Element (FE) methods using THIN-WALL and ABAQUS software, respectively. The ambient temperature compression capacity, normalised to the squash load, was used as the governing parameter to compare the structural efficiencies of the three sections. For elevated temperature analysis, three common LSF wall configurations shown in Table 1 were modelled with LCS, LSB and SCS stud sections, resulting in nine FE thermal and structural models each. Full-scale fire tests of three LSF wall configurations made of LCS studs

[5,15] were used as the basis for validating the thermal and structural FE models. Extended FRL versus Load Ratio plots were developed for each stud section and wall configuration using a combination of steady state and transient state coupled temperature-displacement analyses in ABAQUS. Using these results, this paper also highlights the possibility of structural failure of non-load bearing walls in fire, in particular cavity insulated walls.

2. Finite strip analysis

Elastic buckling analyses of the three sections shown in Fig. 2 were conducted using the finite strip analysis program THIN-WALL, accounting for the plasterboard restraints available at the screw connections on both sides. Screw restraints were simulated as continuous longitudinal translational restraints in the X direction at the locations shown in Fig. 2 for each section. Considering the ability to provide double connectivity to the LSB and proposed SCS stud flanges, these lateral restraints were also provided to the inner flanges of these two sections. The provision of these lateral restraints eliminated the possibility of global buckling about the minor axis, as evident from Fig. 3. These critical buckling shapes correspond to the signature curves shown in Fig. 4 for each of the sections. The section depth was fixed at 90 mm, and the radius at each corner was taken to be twice the thickness of the stud. Design guidelines specify a minimum flange width of 32 mm for plasterboard sheathed stud sections [16]. However, finite strip analyses and subsequent Direct Strength Method (DSM) based calculations showed that a flange width of 40 mm provides greater efficiency, with a higher ultimate failure load, normalised to squash capacity. Hence, a

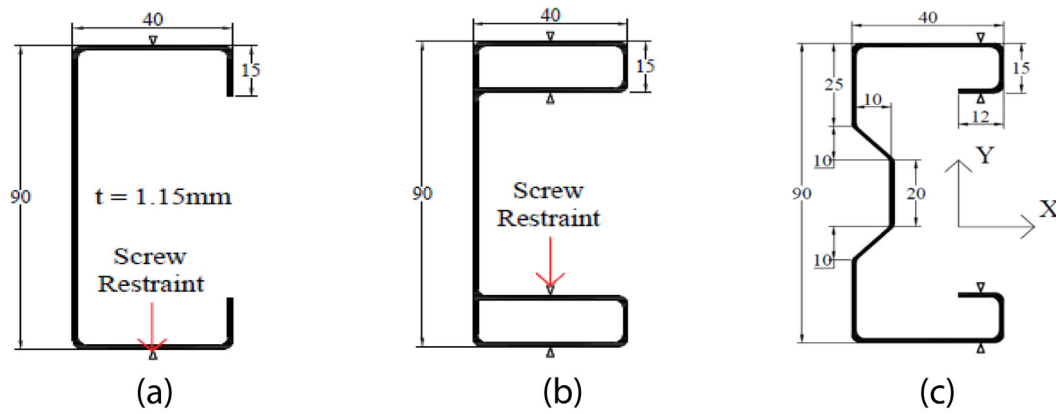


Fig. 2. Stud sections considered in this study (a) LCS, (b) LSB, (c) SCS.

Table 1

LSF wall configurations considered in this study.

Wall Configuration	Insulation Material	Experimental Results [5,15]	
		Load Ratio	FRL (min)
WC 1	None	0.2	53*
WC 2	None	0.2	111*
WC 3	Rockwool (Cavity)	0.2	107

* Fire side plasterboard fall-off exposed the stud to high temperatures, resulting in failure.

flange width of 40 mm was used in this study. While the steel thickness and yield stress were assumed as 1.15 mm and 300 MPa, respectively, the elastic modulus of steel was taken as 200,000 MPa.

Local buckling of the web is a common failure mode prevalent in both LCS and LSB stud sections used in LSF walls. Elastic buckling analyses of these sections revealed the significance of this failure mode, as shown in Fig. 4. The elastic local buckling loads of the LCS and LSB sections are 38 and 123 kN, respectively. A similar analysis of the SCS revealed that local web buckling is eliminated, thus making global buckling about X-axis the predominant mode of failure for this section. The elastic local buckling load of the SCS is 237 kN with a buckling stress of 920 MPa, which confirms that this local buckling mode will not occur.

Elimination of the local buckling mode with the provision of longitudinal web stiffeners in thin-walled sections generally makes the distortional buckling mode to become dominant. This mode is more sensitive to imperfections and has reduced post-buckling capacity [17]. However, the buckling stress of the SCS corresponding to distortional buckling mode was also found to be greater than the material yield strength (300 MPa). Elimination of both local and distortional buckling modes simplifies the structural behaviour of the SCS stud. This will have favourable implications when developing design guidelines for LSF walls made with SCS studs.

The suitability of DSM for the ultimate compression capacity evaluation of optimised sections was highlighted by Schafer [18]. The ultimate capacities of the three sections were evaluated using the DSM guidelines and are presented in Table 2. Normalisation of the ultimate capacity to squash load for each section indicates that the performance of the SCS is superior to that of the LCS and equivalent to the LSB.

FE structural models were also developed to obtain the ambient temperature ultimate compression capacities of the three sections. These were subsequently used in the elevated temperature analyses when calculating the load ratios, defined as the applied load in fire divided by the ambient temperature compression capacity. Furthermore, the FE analyses results were compared with THIN-WALL analyses results and DSM predictions. As seen in Table 3, the critical buckling loads obtained from ABAQUS linear buckling analysis are in good agreement with the THIN-WALL predictions given in Table 2. The DSM predictions of the ultimate failure load, however, were conservative compared to the FE analyses predictions.

3. FE model development

Development of accurate thermal and structural models forms the basis of numerical studies of LSF walls exposed to standard fire on one

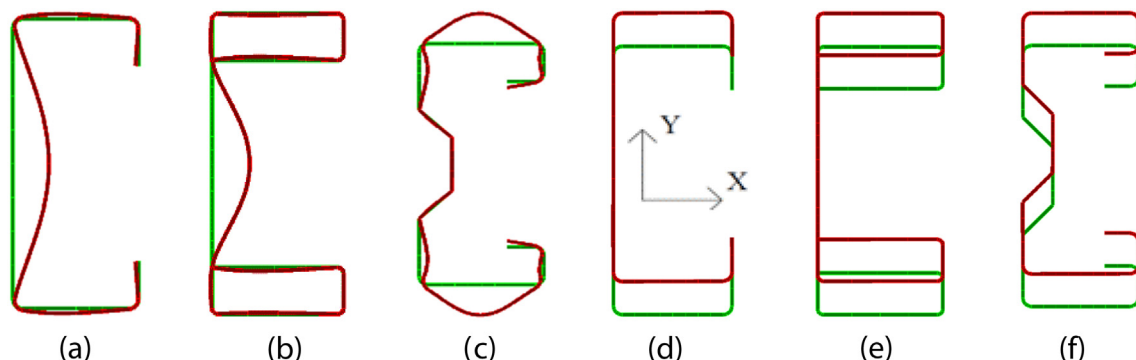


Fig. 3. Critical buckling profiles of sections (a) LCS-Local, (b) LSB-Local, (c) SCS-Local, (d) LCS-Global, (e) LSB-Global, (f) SCS-Global.

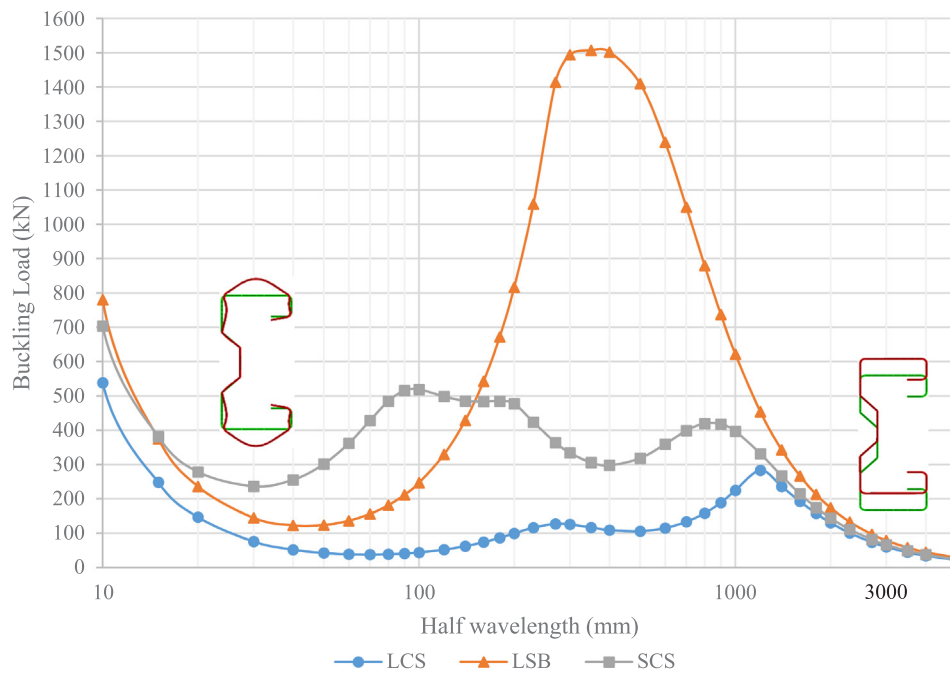


Fig. 4. Buckling load versus half-wavelength curves from THIN-WALL.

Table 2

DSM predicted ultimate compression capacities for the three sections.

Description	LCS	LSB	SCS
Area of section (mm ²)	219	308	251
Squash load (kN)	66	92	75
Critical local buckling load (kN)	38	123	232
Critical global buckling load (kN)	60	79	65
Ultimate compression capacity (kN)	34	57	46
Ultimate capacity/Squash load	0.52	0.61	0.62

Table 3

Ambient temperature ABAQUS FE analysis results for the three sections.

Description	LCS	LSB	SCS
Critical buckling load (kN)	38 (Local) 63 (Global)	81 (Global)	68 (Global)
Ultimate failure load with imperfections (kN)	43	63	53
DSM prediction/ABAQUS prediction	0.79	0.90	0.87

side. A sequentially coupled 3-D analysis was conducted by developing FE thermal and structural models of the three LSF wall configurations identified in Table 1. Each wall configuration was modelled with LCS, LSB, and SCS stud sections, resulting in nine FE thermal models. These were validated using past experimental results [5,15]. Time-temperature profiles for the hot flange (HF) and cold flange (CF) of the studs were extracted from the validated FE thermal models and used in the corresponding FE structural models in the second stage of the sequentially coupled analyses. Nine FE structural models were developed considering the 3 m high LSF wall studs, incorporating the lateral restraints provided by the plasterboards on both sides at the screw locations.

In the sequentially coupled analysis used, the heat transfer analysis is conducted prior to the structural analysis to generate the temperature regime of the stud, which is subsequently applied to the studs to obtain their structural response. Hence, the heat transfer analysis only solves for the thermal progression across the wall. To this end, the mechanical properties of plasterboard are not incorporated. This method relies on

the assumption that although the effect of temperature development of the system on its structural response is significant, the effect of the structural response on the temperature development is low and can be indirectly incorporated with the modification of plasterboard thermal properties, specifically its conductivity (hence, the uncoupled behaviour). The following sections discuss the FE model development for thermal and structural analyses.

3.1. FE thermal modelling

DC3D8 is a 3-D eight-node linear heat transfer brick element with one degree of freedom per node. It was used to model steel studs, plasterboards and insulation materials in FE thermal analyses. A 25 mm x 25 mm mesh size and a 4 mm through thickness were used for the plasterboard mesh. A 25 mm mesh size was also selected for the studs. Surface-to-surface tie constraints were defined between the identified contact pairs to allow for solid-to-solid heat transfer. The ambient temperature was defined as 20 °C over all the elements in the models. ISO 834 [19] standard fire curve was defined as an amplitude and assigned to the fire side of the wall as a boundary condition. Fig. 5(a) illustrates the stud-plasterboard assembly of WC 1 (Table 1) with LCS studs. Mesh arrangements for WC 1 and a lipped channel section are shown in Fig. 5(b) and (c), respectively. Points A1 to A3 and B1 to B3, identified in Fig. 6, are the locations at which the plasterboard temperatures were extracted for subsequent discussions.

Thermal conductivity, specific heat, and relative density properties of gypsum plasterboards were proposed by different past studies [20–22]. Plasterboard thermal properties used in this study are shown in Fig. 7 [22]. As the heat transfer analysis is incapable of directly simulating the mechanical process of plasterboard cracking, this is achieved indirectly with the modification of measured plasterboard thermal conductivity at high temperatures. The sharp rise at 900 °C in the thermal conductivity curve shown in Fig. 7(a) allows the rapid progression of heat across the plasterboard and elevates the stud temperatures. The objective is to simulate the exposure of studs to heat flow following the cracking and fall-off of plasterboard in testing. The calcination process in plasterboard results in two initial peaks in the specific heat curve. These have been accounted for, at 140 °C and 170 °C temperatures, respectively, as shown in Fig. 7(b). The loss of free and

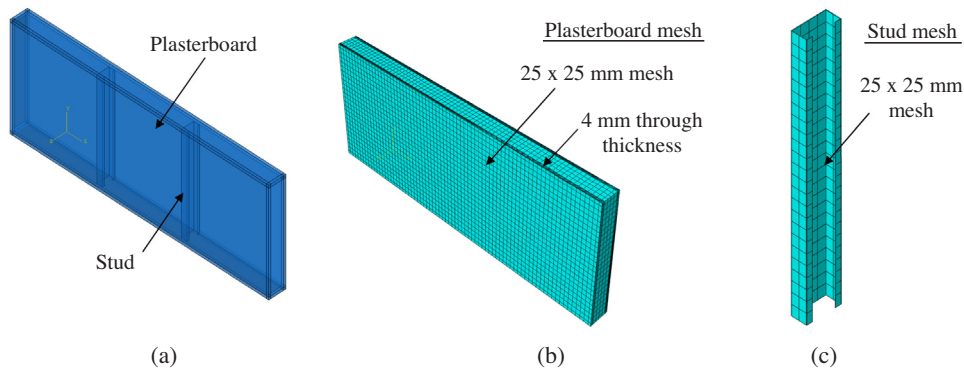


Fig. 5. FE thermal modelling of LSF wall assembly (a) Stud-plasterboard assembly, (b) Plasterboard mesh, (c) Stud mesh.

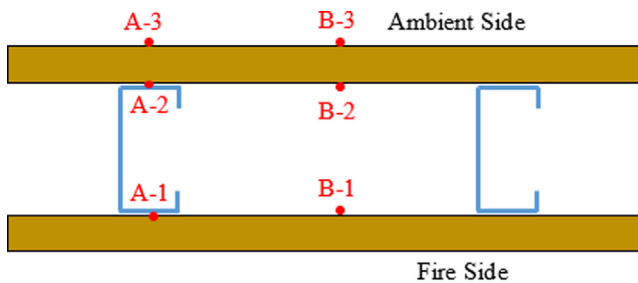


Fig. 6. Plasterboard temperature extraction points.

measured by Keerthan and Mahendran [21] was used in this study and is shown in Fig. 7(d). Thermal properties of steel were introduced using the equations specified in EN 1993-1-2 [13].

Defining the thermal conductivity properties of the materials used allows the model to account for heat transfer through conduction. To simulate convection and radiation heat transfer mechanisms, suitable emissivity and convective coefficients need to be assigned to the surfaces of the LSF wall assembly. An emissivity coefficient of 0.9 was specified for the fire and ambient sides of the plasterboard assembly. Cavity radiation was introduced with an emissivity factor of 0.9 on all cavity surfaces as all of them were plasterboard surfaces. Due to the limited depth of the wall cavity (90 mm), the air inside the wall cavity was assumed as static air and the convective heat transfer within the cavity was therefore not considered. Convection coefficients of 25 and 10 W/(m²°C) were used on fire exposed and ambient surfaces of the LSF walls to simulate convective heat loss to the outside environment, respectively.

chemically bound water during the calcination process results in a loss of mass in plasterboard. The result is a reduction in the relative density as depicted in Fig. 7(c). Plasterboard density at ambient temperature is taken as 780 kg/m³. For Rockwool insulation, specific heat and density were taken to be 840 J/(kg °C) and 100 kg/m³, respectively [21]. Temperature dependent variation of the conductivity of Rockwool

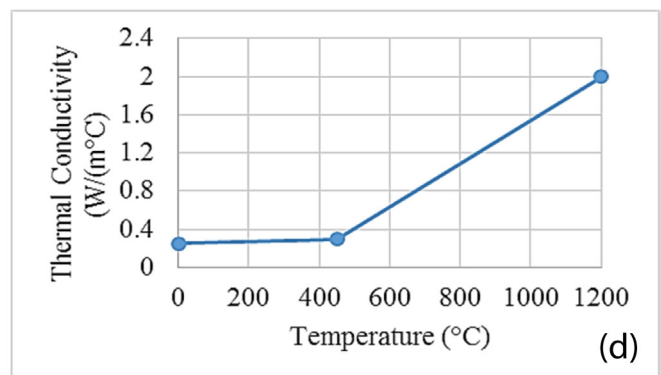
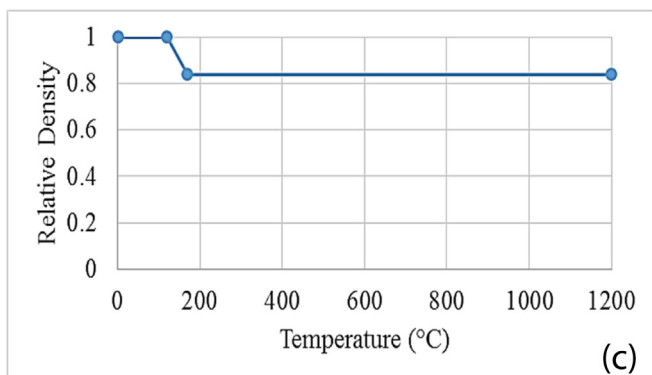
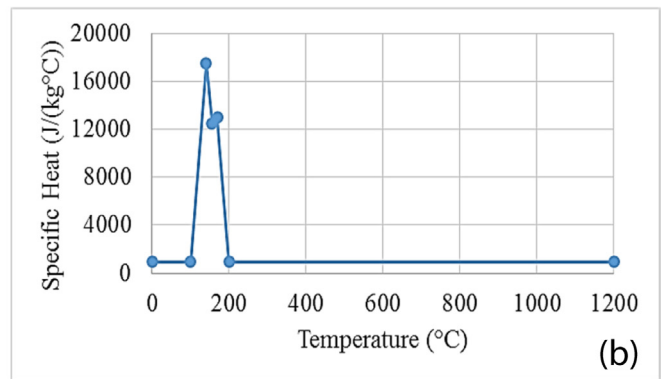
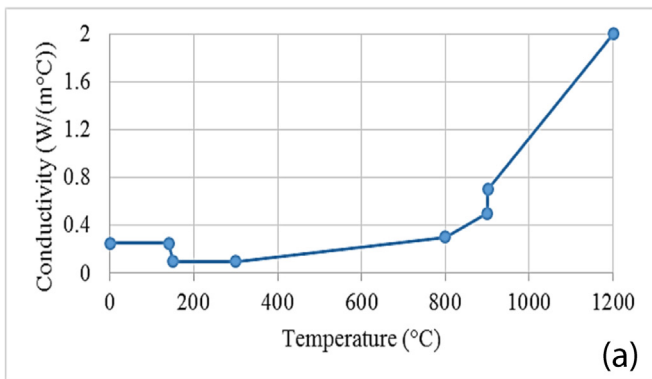


Fig. 7. Thermal properties [20–22] (a) Conductivity-Plasterboard, (b) Specific heat-Plasterboard, (c) Relative density-Plasterboard, (d) Conductivity-Rockwool.

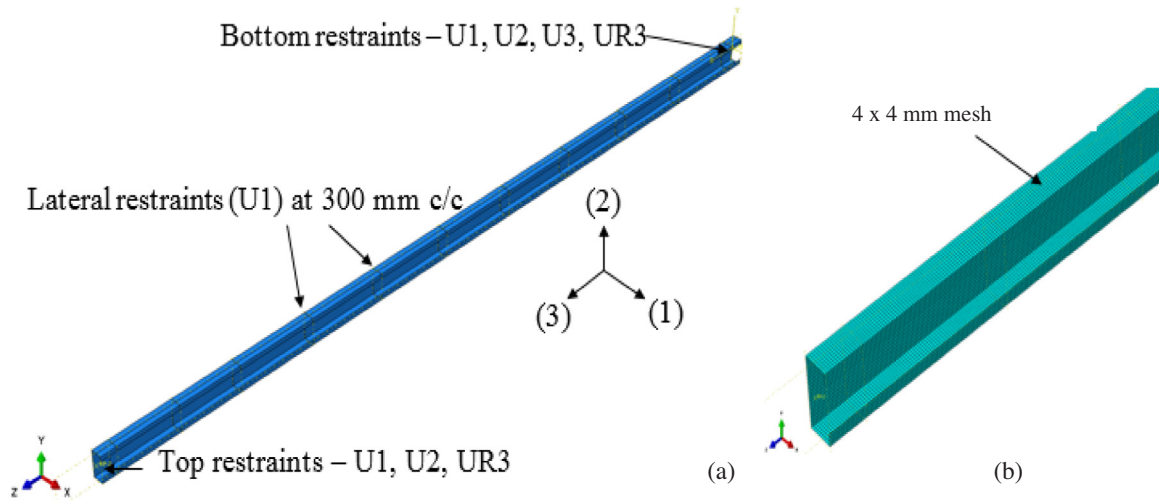


Fig. 8. FE structural model (a) Boundary conditions, (b) Mesh arrangement.

3.2. FE structural modelling

S4R is a general purpose four-node quadrilateral conventional shell element with linear interpolation and reduced integration. It is computationally inexpensive due to having one integration point and has been found to yield closer results as S4 elements in previous FE analyses of LSF walls [12]. S4R elements were used to model the 1.15 mm thick 3 m long studs. Plasterboards were not modelled explicitly, but the effect of screws was simulated as translational restraints in the X direction, as shown in Fig. 8(a). Reference points, coincident with the centroid of the section, were defined at either end of the stud. The end nodes were then constrained to their respective reference nodes using MPC-beam type constraints. Stud top and bottom boundary conditions were applied to these reference points as shown in Fig. 8(a). U1, U2, and U3 refer to the axial restraints in the X, Y and Z directions, respectively. The rotational restraints about these axes, in the same order, are UR1, UR2, and UR3. At the bottom reference point, translations about X, Y and Z axes and rotation about Z-axis were restrained. Similar boundary conditions were specified at the top, but the translational restraint in the Z direction was released to allow for axial shortening. The load was applied at the top reference point.

A mesh size of 4 mm × 4 mm was used to discretise all the studs as illustrated in Fig. 8(b). As stated earlier, a nominal yield strength of 300 MPa and an elastic modulus of 200,000 MPa were considered at 20 °C ambient temperature for steel studs. Reduction factors for yield strength and elastic modulus of low strength steels proposed by Kankanamge and Mahendran [23] were used to determine elevated temperature mechanical properties. Poisson's ratio of steel was assumed to be 0.3. The density of steel was taken as 7850 kg/m³. Thermal properties of steel were defined using the equations specified in EN 1993-1-2 [13]. Gunalan and Mahendran [12] and Kesawan and Mahendran [14] used similar idealisations in their FE analyses of LCS and LSB studs, respectively.

Eigen modes obtained from the linear buckling analyses were used to introduce the geometric imperfections into the models in non-linear analyses using the *IMPERFECTION card. The first Eigen mode of LSB and SCS was the global buckling mode. The imperfection magnitude pertaining to this mode was taken to be L/1000, where L is the member length. However, for the LCS, the initial Eigen modes were all related to local buckling of its slender web. The global buckling mode appeared as a higher order Eigen mode. Thus, for the LCS, both local and global buckling modes were used to introduce imperfections in the non-linear analyses. Imperfection magnitude for local buckling was taken as b/150, where b is the width of the most slender element. This behaviour was expected for the LCS as the THIN-WALL analyses (Section 2)

indicated the occurrence of local-global interaction in the LCS, as seen in Fig. 4.

Average stud HF and CF time-temperature profiles extracted from the results of the FE thermal analyses were assigned to the stud HF and CF. Linear temperature variations were assumed along the web for all the stud sections, and these idealised temperature distributions are shown in Fig. 9. Axial loads pertaining to each load ratio considered were calculated based on the ambient temperature compression capacity of each stud (Table 2) and assigned at the stud centroid. These loads were maintained while the nodal temperatures were increased under transient state FE analyses. The model accounted for the degrading mechanical properties of steel, and failure occurred when the applied load could not be maintained any further.

The common loading range for load bearing LSF walls, expressed in terms of load ratio, is between 0.2 and 0.7. Therefore, a comprehensive analysis of the FRL of all the LSF walls considered was done within this range. To gain a better understanding of the lightly loaded and heavily loaded LSF walls, the analysis was subsequently further extended for a set of selected walls. FRLs for load ratios up to 0.7 were found using transient state coupled temperature-displacement analysis. Due to the convergence problems associated with higher load ratios, steady state analysis was used at selected time points corresponding to high load ratios. Steady state analysis was conducted in two steps. In step one, the temperatures across the stud were elevated to the required level. The axial compression load was then applied, in step two, as a linearly increasing force, until failure.

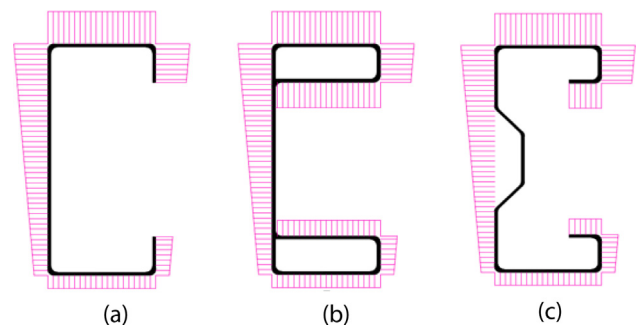


Fig. 9. Idealised non-uniform temperature distributions (a) LCS, (b) LSB, (c) SCS.

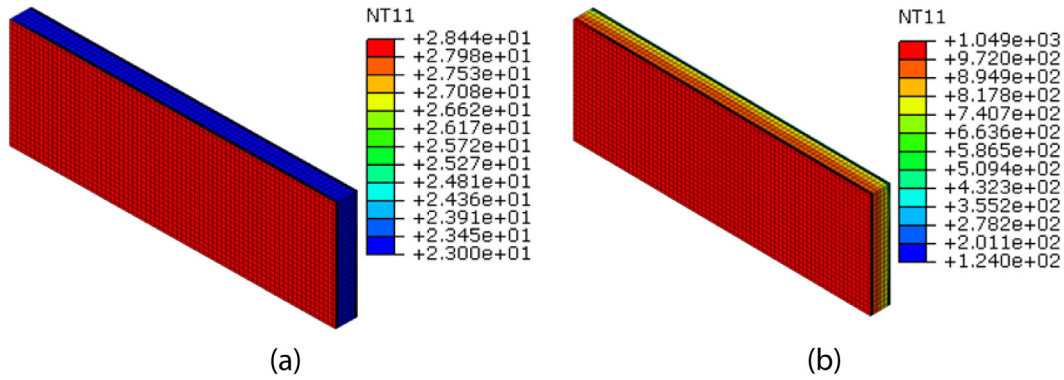


Fig. 10. Heat progression in WC 1 (a) $t = 1$ s, (b) $t = 2$ h.

4. FEA results and discussion

4.1. FE thermal modelling results

Fig. 10(a) illustrates the commencement of temperature rise on the fire side plasterboard surface in a single plasterboard lined LSF wall model (WC 1 in Table 1). Plasterboard temperatures after a two-hour fire exposure is shown in Fig. 10(b). Fig. 11 shows the stud mid-height HF and CF time temperature variations for LCS, LSB and SCS studs in WC 1 exposed to standard fire on one side. HF and CF time-temperature variations are found to be independent of the stud geometry with a temperature difference of only up to 20 °C among the three stud sections at any given time. Similar observations were also made for WCs 2 and 3 as well.

Average stud time-temperature profiles obtained from FE thermal models matched well with the experimental results of Kolarkar [15] for all three wall configurations considered, as shown in Fig. 12. Fig. 12(a) and (b) show sudden rises in experimental stud temperature profiles due to the formation of cracks and the subsequent plasterboard fall-off. However, the stud time-temperature profiles for WC 3, shown in Fig. 12(c), indicate no fall-off.

4.2. Insulation failure in non-load-bearing LSF walls

In this section, plasterboard time-temperature profiles from the validated FE thermal models are used to predict the insulation failure based FRL of non-load bearing LSF walls using the insulation failure criteria given in AS 1530.4 [24].

- Average temperature of the unexposed surface exceeds the ambient temperature by more than 140 °C.
- Temperature at any location on the unexposed surface exceeds the ambient temperature by more than 180 °C.

The average temperature based insulation failure time was found to

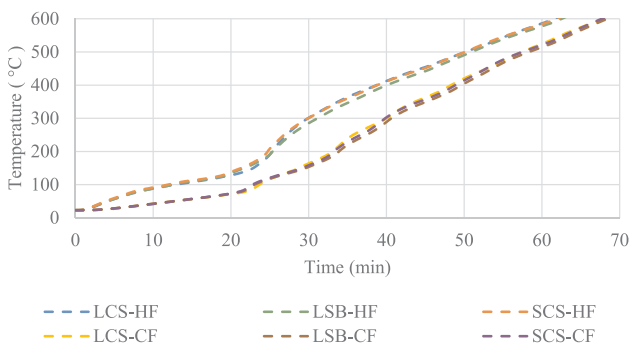


Fig. 11. Stud HF and CF time-temperature profiles for WC 1.

be critical in all the wall configurations. The average plasterboard temperatures were calculated using the plasterboard ambient surface top level, mid-height and bottom level temperatures. These average plasterboard temperature variations are shown in Fig. 13. Table 4 presents the insulation failure times of WCs 1 to 3 from thermal FE analyses, which agree well with the manufacturer specified insulation based FRLs. These insulation failure times are equally applicable to all three stud sections, as the stud geometry was found to have minimal influence over the temperature development across the wall.

Fig. 13 shows that in non-insulated walls (WCs 1 and 2), the average ambient side plasterboard temperatures at the centre of the wall (Point B-3 – located between the studs in Fig. 6) are slightly higher than those at the stud location (Point A-3) throughout the analysis duration. The maximum difference between the two curves at any temperature is only about 3 min. However, in the cavity-insulated wall (WC 3), the average ambient side plasterboard temperature at Point A-3 is noticeably higher than that at Point B-3 throughout the analysis. In fact, the difference between the two curves increases with time. Thus, if the FRL of a non-load bearing cavity insulated wall was determined based on the average ambient side plasterboard temperature at the centre of the wall (B-3), the FRL would be overestimated. This is clearly shown in Table 4, where the times taken to reach the critical average temperature of 160 °C at A-3 and B-3 are presented for each wall configuration. As per the results, for non-cavity insulated walls (WCs 1 and 2), temperatures at B-3 give conservative FRLs of 81 and 194 min. However, for WC 3, the FRL estimation based on B-3 temperatures (300 min) is 26 min greater than that based on A-3 temperatures.

To gain a better understanding of the heat progression across the wall and its effects on plasterboard temperatures, individual plasterboard nodal temperatures measured at wall mid-height are plotted in Fig. 14(a) and (b) for WCs 2 and 3, respectively. A direct comparison between these two configurations is worthwhile as they both have the same double plasterboard configuration. Clearly, a difference is

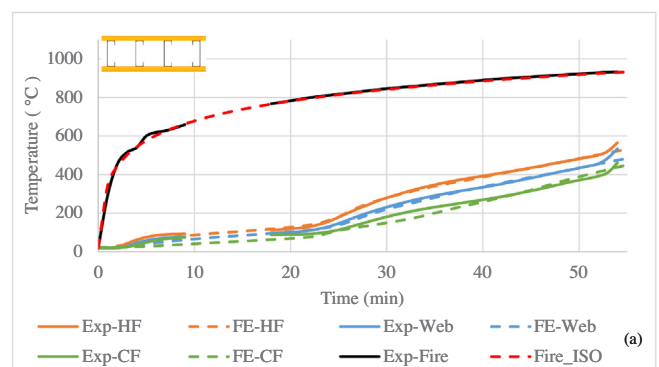


Fig. 12. FE model validation (a) WC 1, (b) WC 2, (c) WC 3.

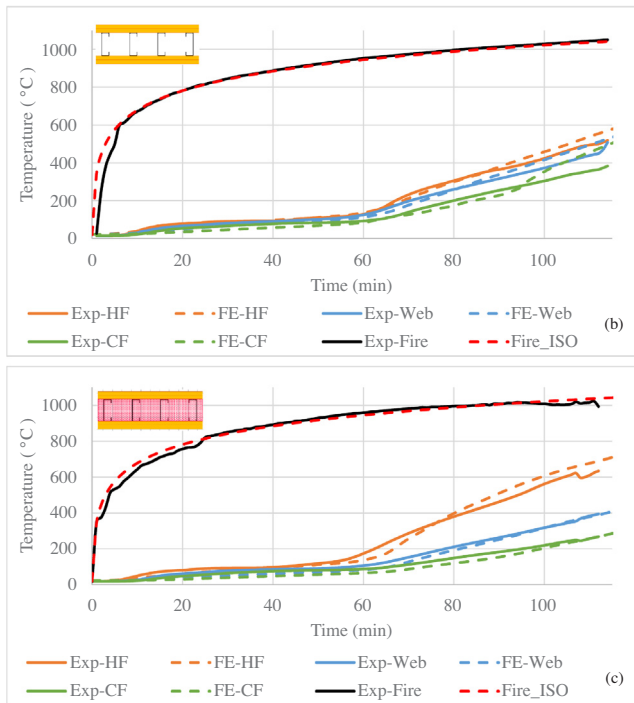


Fig. 12. (continued)

observed in the plasterboard temperature variations between the two wall configurations. The following section is intended to explain this difference between plasterboard temperature variations observed in insulated and non-insulated LSF walls. The basic notion is that alteration of the heat transfer mechanism across the wall, with the provision of cavity insulation in WC 3, has a profound impact on the magnitude and progression of the heat passing through the wall. The conductivity of steel is taken to be 54 W/(m °C) at ambient temperature and reduces to 27.3 W/(m °C) at elevated temperatures [13]. In contrast, the conductivity values of plasterboard and Rockwool are much smaller, ranging between 0.25 and 2 W/(m °C) (Fig. 7). This makes the heat progression non-uniform across the wall width as the studs are located intermittently, spaced 600 mm apart. In WC 3, heat energy would pass

through the studs with relative ease, creating intermittent thermal bridges within the wall.

In a non-cavity insulated wall, the heat front, once it reaches the inside of the fire side plasterboard (Points A-1 and B-1), can progress via radiation mode across the cavity and conduction mode through the stud. Thermal radiation occurs in the form of electromagnetic waves, which travel at a speed of 3×10^8 m/s through a vacuum and a slightly reduced speed in the presence of air. This results in an immediate heat gain by the ambient side plasterboard across the cavity (Point B-2). However, the high conductivity of steel also causes heat to flow rapidly across the steel stud to the ambient side plasterboard (Point A-2). In fact, as shown in Fig. 14(a), the temperature at Point A-2 is greater than that at Point B-2 up to 58 min. This is attributed to the high conductivity of steel. With time, however, steel conductivity reduces, and thermal radiation causes the plasterboard temperature at Point B-2 to surpass that at Point A-2. These two phenomena together result in the observed variations in the ambient side plasterboard temperatures of the FEA results. It is evident, as seen in Fig. 14(a), that eventually radiation heat transfer across the cavity marginally exceeds conduction heat transfer across the stud as ambient side plasterboard temperatures at Points B-1 to B-3 are slightly greater than those at Points A-1 to A-3.

A cavity-insulated LSF wall eliminates the existence of an air cavity, resulting in the elimination of thermal radiation. However, a new mode of heat transfer is introduced in the form of conduction through cavity insulation. The conductivity of Rockwool is significantly lower than that of steel. Therefore, the heat front, once it reaches the inner surface of the fire side plasterboard, travels much faster to the ambient side plasterboard through the steel stud than through the Rockwool insulation. This fact is illustrated in Fig. 14(b), where plasterboard temperature at Point A-2 is greater than that at Point B-2 throughout the analysis for WC 3. This is different from the plasterboard temperature variations at the same two points in the non-insulated wall (WC 2) shown previously in Fig. 14(a). However, the conductivity of plasterboard is also much smaller than that of steel. Thus, the heat energy that reaches the cold flange of the stud at a rapid rate now has to progress into the plasterboard at a much lower rate. This results in an isolated heat build-up near the CF, as shown in Fig. 15(a). The Rockwool insulation has been deactivated here for improved clarity of the figure. Fig. 15(b) shows that despite another local heat build-up occurring at the centre of the wall due to conduction through the Rockwool cavity insulation, the ambient side plasterboard temperature at Point B-3 is

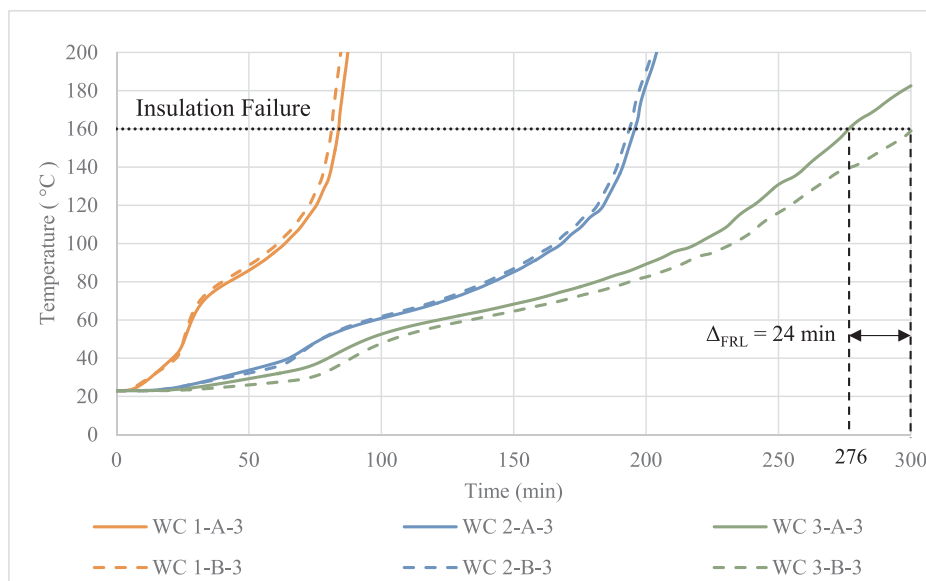


Fig. 13. Average ambient side plasterboard temperature variations.

Table 4
Insulation failure times of non-load bearing walls.

Wall Configuration	FEA Insulation Failure Time (min)		Manufacturer specified, Insulation based FRL (min) [25]
	A-3	B-3	
WC 1	84	81	90
WC 2	196	194	180
WC 3	276	300	–*

* A reliable FRL for Rockwool cavity insulated, double plasterboard lined wall is not available.

lower than that at Point A-3.

Based on the above analyses and discussions, it can be stated that in non-insulated walls such as WCs 1 and 2, the location where the ambient surface temperature is measured would not have much influence over the insulation based FRLs. However, the insulation based FRLs of cavity insulated walls should be determined based on the ambient side plasterboard temperatures over the studs, due to the formation of

thermal bridges and the resulting localised temperature rise in plasterboard in the vicinity of studs.

4.3. FE structural modelling results

Linear buckling and non-linear analyses of 3 m long columns at ambient temperature enabled the determination of ambient temperature ultimate capacities of the three studs. These are 43, 63 and 53 kN for the LCS, LSB and SCS sections, respectively (Table 3). The load ratios were calculated using these values in the subsequent elevated temperature FE analyses.

FRL (failure time) variations of load bearing LSF walls with load ratios in the range of 0.2 to 0.7 are presented in Fig. 16. Given that the stud time-temperature profiles are similar for different stud geometries (Fig. 11), the FRL values also tend to match closely. This implies that under fire conditions, the three studs will perform similarly when subjected to the same load ratio. Shown in Fig. 17 are the failure modes obtained for WC 1 with a 0.6 load ratio. These modes were typical for the three sections. Ultimate failure occurs due to major axis global buckling in all cases. Additionally, the failure mode of LCS shows the

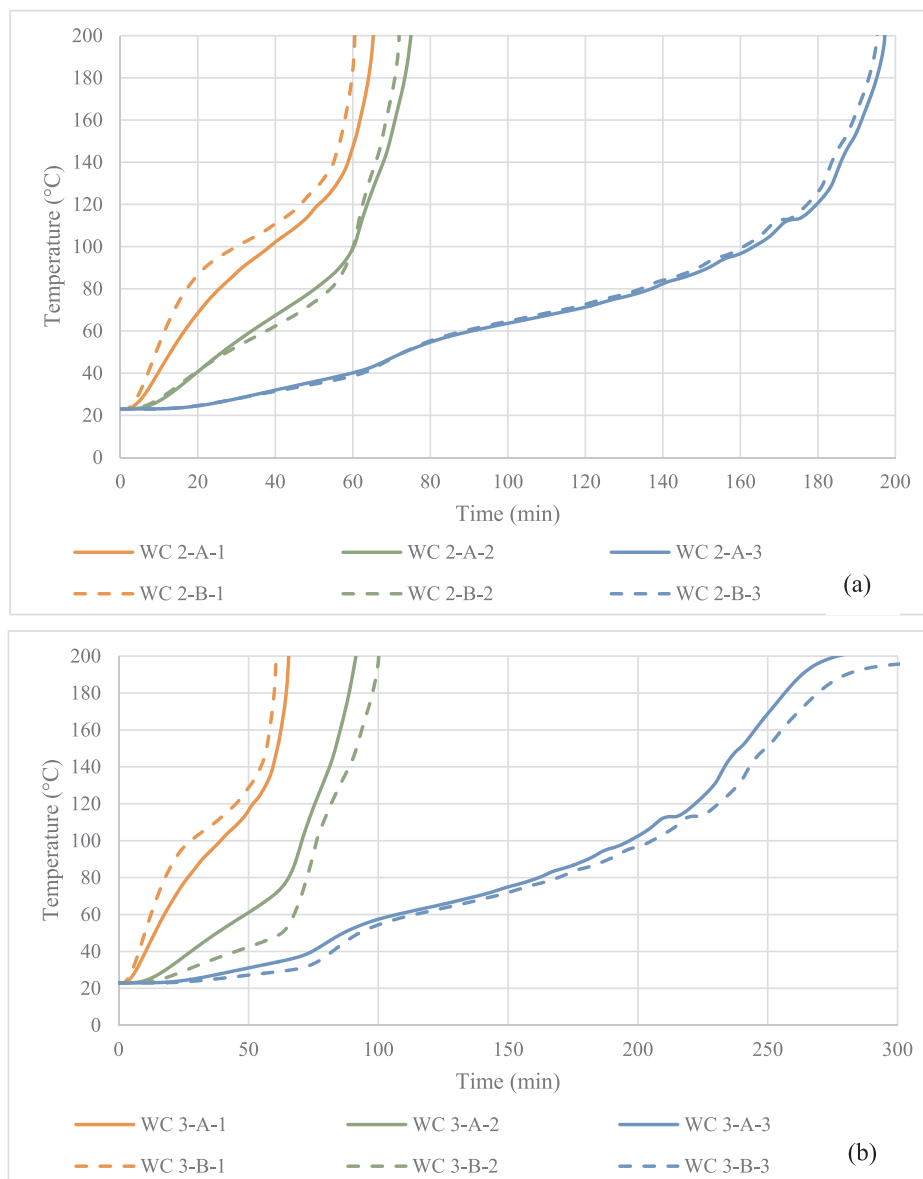


Fig. 14. Individual plasterboard mid-height temperature variations (a) WC 2, (b) WC 3.

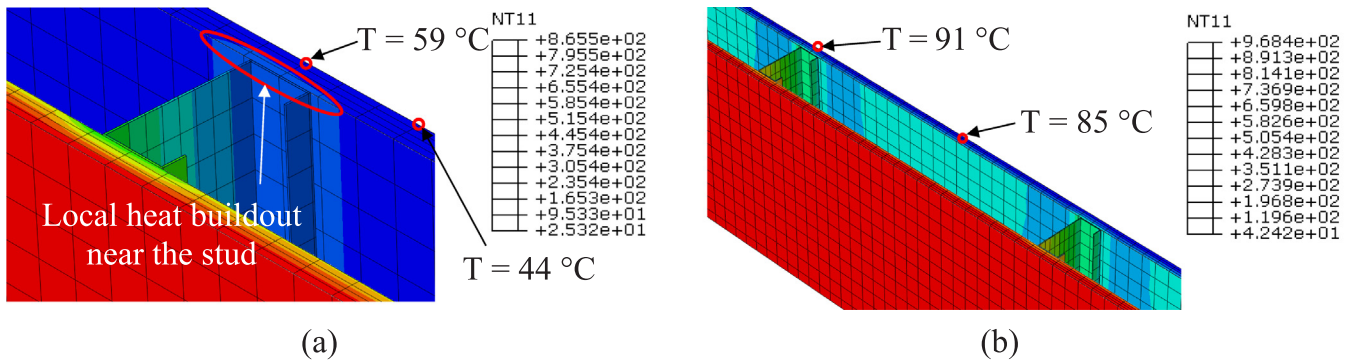


Fig. 15. Localised heat build-up near cold flange in WC 3 (a) $t = 35$ min, (b) $t = 70$ min.

development of local buckling waves along its slender web.

The experimental failure times for WCs 1, 2 and 3 with 0.2 load ratio are 53, 111 and 107 min, respectively [15]. The corresponding failure times from the FE structural models are 66, 123 and 98 min, respectively. The differences between the experimental and numerical failure times can be attributed to the following: (1) the use of nominal section and mechanical properties (2) not considering the residual stresses (3) the use of nominal geometric imperfection values. The above assumptions were used in FE analyses as the focus of this study was to compare the performance of the three stud sections in LSF walls. It should also be noted that WCs 1 and 2 showed plasterboard fall-off near failure in the fire tests, which reduced their failure times.

Developing the FRL versus Load Ratio plot across the entire spectrum of load ratios is important to fully understand the behaviour of LSF walls. FRL values obtained for the three wall configurations using steady state coupled temperature-displacement analysis at high load ratios were thus combined with previous analysis results and are presented in Fig. 18. Insulation failure criteria have also been incorporated into the FRL versus Load Ratio plot to provide an upper limit to the FRL

of non-load bearing LSF walls. The analysis was limited to walls with LCS stud sections as it has already been established that elevated temperature performance of the studs is independent of the stud geometry. Additionally, to account for the very lightly loaded LSF walls, the analysis was first extended to 0.05 load ratio. Transient state analysis with a load ratio of 0.05 indicated that only WC 1 meets the insulation failure criteria. Therefore, WC 2 was reanalysed with a load ratio of 0.03, and was found not to fail structurally even at 240 min. The analysis was terminated at this stage, given that insulation failure criterion is met at 194 min. Similarly, the analysis was extended to 0.03 and 0.015 load ratios for WC 3, which showed that WC 3 did not fail structurally at 0.015 load ratio, even after 300 min of fire exposure. Some of the results for these very small load ratios are given in Table 5.

The effect of cavity insulation on the overall fire performance of LSF walls has been investigated before [12,22]. Using FE structural models, it is shown in this study that for load ratios higher than 0.6, the FRL of insulated and non-insulated double plasterboard walls are similar, with non-insulated wall showing marginally better performance (Fig. 18). At the two extremes of the curve, beyond 0.85 and below 0.05 load ratios,

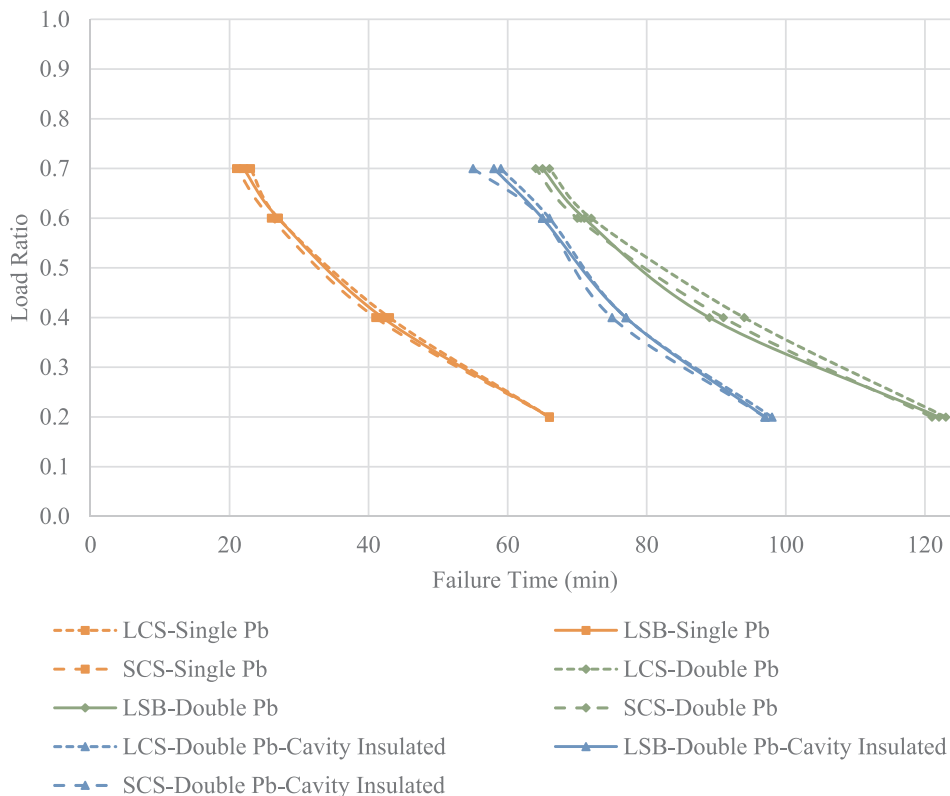


Fig. 16. FRL of LSF walls under common load ratios.

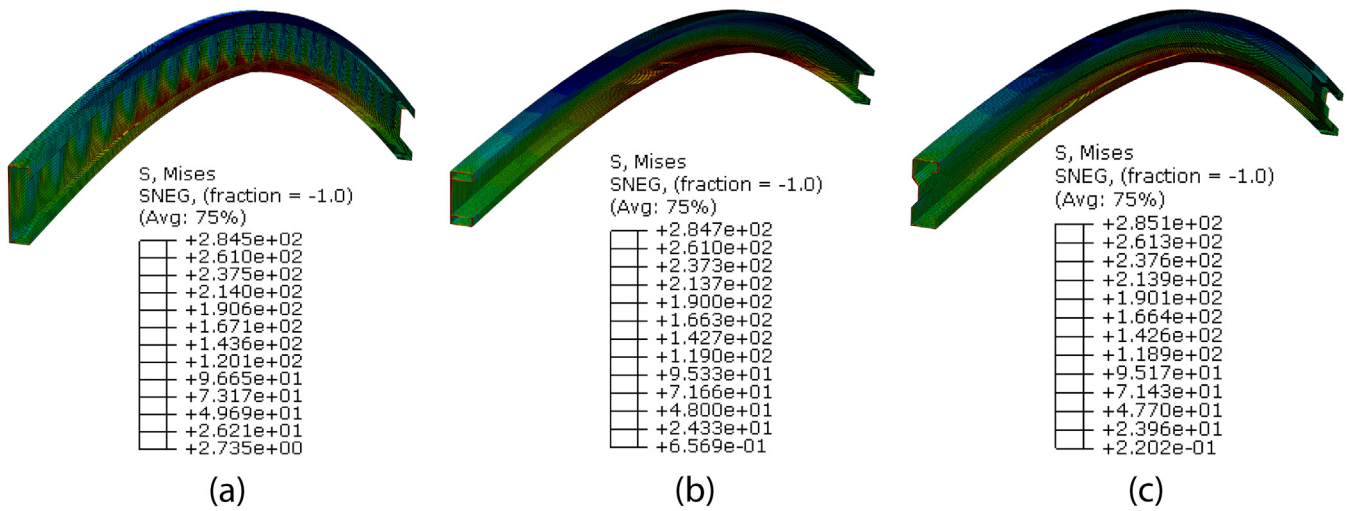


Fig. 17. Ultimate failure modes of WC 1 with 0.6 Load Ratio (a) LCS-Local + Global, (b) LSB-Global, (c) SCS-Global.

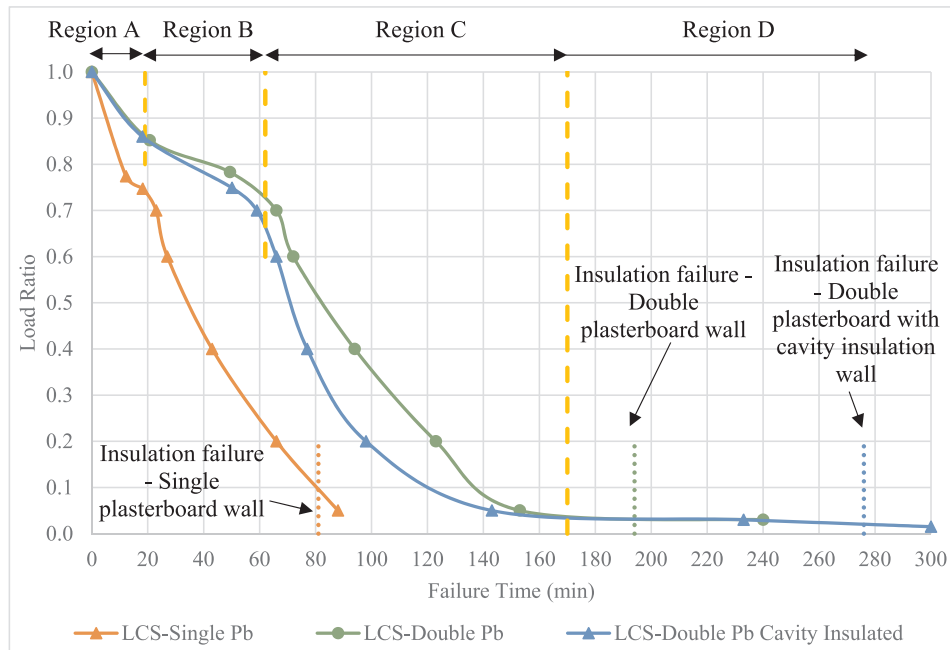


Fig. 18. Extended FRL variations of LSF walls.

Table 5
FRL variation within Region D in double plasterboard walls.

WC No.	Description	Load Ratio	Absolute Load		FRL (min)	FRL Reduction (min)
			kN	kg		
WC 2	Double plasterboard non-insulated wall	0.03	1.29	131	194 (I)	41
		0.05	2.15	219	153 (S)	
WC 3	Double plasterboard cavity-insulated wall	0.015	0.65	66	276 (I)	133
		0.05	2.15	219	143 (S)	

I-Insulation failure, S-Structural failure

the FRL values are identical for the two types of walls.

The following discussion on the extended FRL versus Load Ratio plots shown in Fig. 18 draws reference to the stud hot flange

temperature profiles presented in Fig. 12. Specifically, WC 2 is used to explain the behaviour of the walls under different load ratios. For improved clarity, stud HF temperature variation for WC 2 is presented in Fig. 19 to explain the correlation between the stud temperature and FRL.

Regions A, B, C and D in Fig. 19 correspond to the four distinguishable regions of the FRL versus Load Ratio plot of WC 2. Regions A and C, which exhibit steep gradients in Fig. 18, correspond to the regions in the stud HF time-temperature profile which exhibit sharp rises in temperature as seen in Fig. 19. Region B relates to the calcination process of plasterboard, where the free and chemically bound water is evaporated, consuming energy. It results in a stagnation in the stud HF temperature rise which materialises into a larger variation in FRL, within a shorter load ratio range. This also means that the variability of FRL of heavily loaded LSF walls with load ratios in the range of 0.7 to 0.85 is high. Accurate prediction of actual loading is necessary to specify a reliable FRL for such a wall. The maturity stage of the fire curve causes another stagnation in the stud temperatures. This region is not reached during the experiment as structural failure of the tested wall

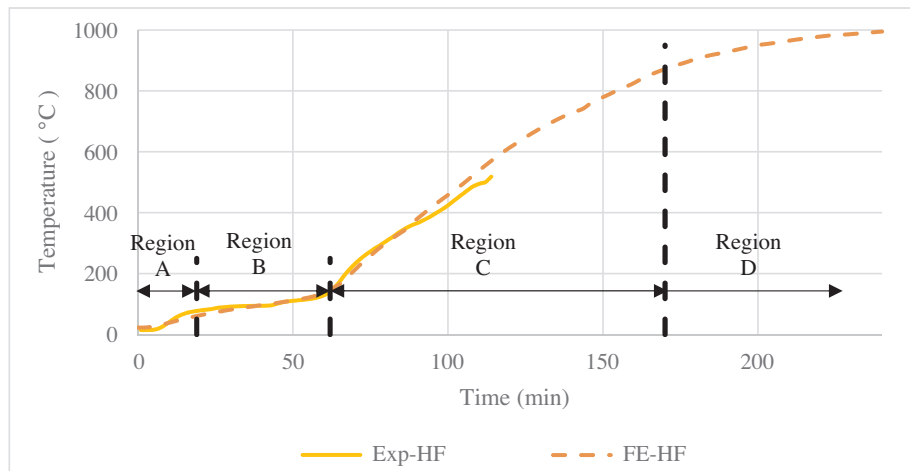


Fig. 19. Relationship between stud HF temperatures and FRL of WC 2.

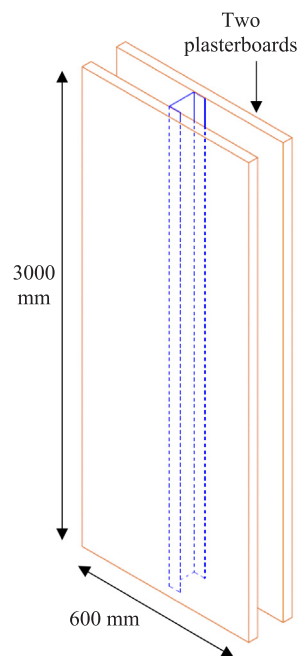
occurred at 111 min. However, the validated FE thermal analysis allows the continuous analysis of the structure which shows that the stud HF temperature also approaches a maturity stage, as shown in Fig. 19. This stage, marked as Region D, indicates that the FRL of the wall can exhibit a great variation, within a very short load ratio range, before being limited by the insulation failure criterion at 194 min. The implications of this are further explained next.

The FRL versus Load Ratio plots of WCs 2 and 3 exhibit a significant FRL variation within a very small load ratio range within Region D. In practice, non-load bearing LSF walls are, at times, used to support door and window frames and additional wall hangings such as shelves. Furthermore, in fire, thermal expansion of the studs also introduces an axial force. As per the findings shown in Fig. 18, especially in cavity-insulated LSF walls intended to be non-load bearing wall, this additional loading may cause premature structural failure of the studs. This is further illustrated in Table 5, where an FRL reduction of 133 min (2 h) is evident for the cavity-insulated double plasterboard lined wall, with the increase of load ratio from 0.015 to 0.05. Furthermore, it should be noted that the absolute load values corresponding to 0.015 and 0.05 load ratios are within the working range of walls used in practice. To illustrate this point further, the loads applied on a non-load bearing wall stud are idealised, and calculated as shown in Fig. 20. W_{pb} and W_{st} refer to self-weights of the plasterboards and steel stud, respectively.

The self-weight of the plasterboards is considered to be transferred to the stud through the plasterboard screws along the stud. The common practice in drywall construction is to raise the plasterboards slightly, without resting them on the floor, and screw them onto the studs. Thus, the weight of the plasterboards and any additional cladding on the plasterboard surfaces will be supported by the studs. The self-weight of the stud is also included in this calculation. Thus, the total self-weight on a non-load bearing stud at ambient temperature will be about 933 N, ie. a load ratio of 0.022. It is, therefore, argued that in the case of a fire, with the presence of thermal expansion, the effective load ratio of a stud will be greater than 0.022. As illustrated in Fig. 18, such an increased load ratio will result in a significant reduction in the FRL of the wall.

4.4. Summary of results

FRLs of the three wall configurations with 0.2 load ratio, obtained from different analyses, are summarised in Table 6. For non-load bearing walls, the average ambient surface temperature was used to determine insulation failure. The manufacturer specified FRL for single and double plasterboard lined non-load bearing walls (WCs 1 and 2, respectively) also agree reasonably well with the FE thermal analysis



Self-weight of four plasterboards

$$W_{pb} = (0.6 \times 3 \times 0.016)m^3 \times 780kg/m^3 \times 4nos$$

$$W_{pb} = 90 \text{ kg}$$

Self-weight of the stud

$$W_{st} = 219mm^2 \times 10^{-6} \times 3m \times 7850kg/m^3 = 5 \text{ kg}$$

$$W_{Total} = 95 \text{ kg} = 933 \text{ kN}$$

Fig. 20. Loads on a stud in WC 3.

predicted values.

Structural failure in load bearing walls could be determined directly from the FE structural models. Alternatively, critical stud hot flange temperatures could also be used [5,15]. As shown in Table 6, the FRLs of load bearing walls determined from these two methods showed good agreement, with a maximum difference of only 6%. Thus, critical stud hot flange temperature based FE thermal model predictions alone can be used to accurately predict the FRL of these three wall configurations, with either type of stud section used.

Future work includes non-load bearing and load bearing fire tests, as well as ambient temperature axial load tests of LSF walls made of SCS

Table 6
Summary of FRLs from different sources.

WC	LR	FRL _{Exp}	NLB-FE _{Thermal}	LB-FE _{Thermal}	LB-FE _{Structural}	NLB [25]	LB [25]
1	0.2	53	81	62	66	–/90/90	60/60/60
2	0.2	111	194	118	123	–/180/180	120/120/120
3	0.2	107	276	99	98	–	–

NLB – Non-Load Bearing; LB – Load Bearing; Exp-Experimental. All values are in mins.

studs to prove the findings of the numerical simulations conducted in this study.

4.5. Overall performance of web-stiffened channel section

Hollow flange sections such as Lite Steel beams (LSB) possess higher torsional rigidity than open channel sections. Hence, they do not suffer from torsional buckling failure modes as evident from the finite strip analyses of LSB (Fig. 4). However, the restraints provided by the plasterboards were able to eliminate such torsional failure modes. Therefore, the additional torsional rigidity provided by the hollow flanges can often be redundant in plasterboard sheathed LSF walls.

Rivet fastened hollow flange channel section provides an alternative to retaining high torsional rigidity while eliminating the high cost of welding along the web-flange joints. However, the ultimate capacity of axially loaded rivet fastened HFC sections was found to be about 40% lower than that of an equivalent welded HFC section [7].

The ultimate compression capacity of the proposed web-Stiffened Channel Section (SCS), normalised to its yield capacity, is equivalent to that of the LSB, and higher than that of the Lipped Channel Section (LCS) at ambient temperature. The cost of manufacturing the SCS, however, will be considerably lower than the production cost of LSB due to the elimination of welding. Its cost of production is likely to be very close to that of the LCS. The stiffened channel section, therefore, provides an economical and structurally efficient alternative to welded and riveted HFC sections, and LCS in LSF wall applications. Since both thermal and structural fire performance analyses of LSF wall studs have shown that the effect of stud geometry is minimal, the three sections will perform similarly in fire for the same load ratio.

5. Conclusion

This paper has presented the details of numerical analyses conducted to study the performance of LSF walls built with three different steel stud sections under both ambient and fire conditions. These studs include the Lipped Channel Section (LCS), welded Hollow Flange Section known as the LiteSteel Beam (LSB) and a new web-Stiffened Channel Section (SCS). The results from this study have shown that the web-Stiffened Channel Section (SCS) has an ultimate compression capacity, normalised to its squash load, equivalent to the LSB and higher than the LCS at ambient temperature. In fire conditions, the stud geometry has minimal influence over the performance of LSF wall studs. Therefore, the SCS was found to match the thermal and structural fire performance of LCS and LSB sections, in LSF wall applications. Since SCS eliminates the necessity for welding or riveting between web and flange, it is more economical to produce, much like the LCS, but is just as efficient as the LSB. Hence this study recommends the use of SCS in LSF wall applications.

The FE models developed here also helped to critically analyse the fire performance of load bearing and non-load bearing walls in fire. An extended FRL versus Load Ratio curve was developed for each of the three LSF wall configurations considered in this study. The Finite Element thermal modelling results showed that insulation failure in cavity-insulated LSF walls should be determined based on the ambient

side temperature at the stud location and not at the centre of the wall. Additionally, this paper highlights the susceptibility of non-load bearing LSF walls failing in fire under structural inadequacy, in particular cavity insulated walls, using the extended FRL versus Load Ratio curves developed.

References

- [1] Fiorino L, Iuorio O, Landolfo R. Designing CFS structures: The new school bfs in naples. *Thin-Wall Struct* 2014;78:37–47.
- [2] Alfawakhiri F, Sultan MA. Fire resistance of loadbearing LSF assemblies. In: 15th International Specialty Conference on Cold-Formed Steel Structures, St. Louis, Missouri, USA, 2000, p. 545–61.
- [3] Gerlich JT, Collier PCR, Buchanan AH. Design of light steel-framed walls for fire resistance. *Fire Mater* 1996;20(2):79–96.
- [4] Feng M, Wang YC. An experimental study of loaded full-scale cold-formed thin-walled steel structural panels under fire conditions. *Fire Saf J* 2005;40(1):43–63.
- [5] Gunalan S, Kolakar P, Mahendran M. Experimental study of load bearing cold-formed steel wall systems under fire conditions. *Thin-Wall Struct* 2013;65:72–92.
- [6] Kesawan S, Mahendran M. Fire tests of load-bearing LSF walls made of hollow flange channel sections. *J Constr Steel Res* 2015;115:191–205.
- [7] Kesawan S, Mahendran M, Dias Y, Zhao W-B. Compression tests of built-up cold-formed steel hollow flange sections. *Thin-Wall Struct*;2017:116(Suppl C) p. 180–93.
- [8] Laím L, Rodrigues JPC, Craveiro HD. Flexural behaviour of beams made of cold-formed steel sigma-shaped sections at ambient and fire conditions. *Thin-Wall Struct* 2015;87:53–65.
- [9] Rodrigues JPC, Laim L, Craveiro HD. Influence of web stiffeners on cold-formed steel beams subjected to fire. *J Struct Fire Eng* 2016;7(3):249–61.
- [10] Shahbazian A, Wang YC. A simplified approach for calculating temperatures in axially loaded cold-formed thin-walled steel studs in wall panel assemblies exposed to fire from one side. *Thin-Wall Struct* 2013;64:60–72.
- [11] Shahbazian A, Wang YC. Direct Strength Method for calculating distortional buckling capacity of cold-formed thin-walled steel columns with uniform and non-uniform elevated temperatures. *Thin-Wall Struct* 2012;53:188–99.
- [12] Gunalan S, Mahendran M. Finite element modelling of load bearing cold-formed steel wall systems under fire conditions. *Eng Struct* 2013;56:1007–27.
- [13] CEN, EN 1993-1-2:2005; Eurocode 3: Design of steel structures; Part 1-2: General rules-Structural fire design, Brussels, Belgium, 2005.
- [14] Kesawan S, Mahendran M. Predicting the performance of LSF walls made of hollow flange channel sections in fire. *Thin-Wall Struct* 2016;98:111–26.
- [15] Kolakar P. Structural and thermal performance of cold-formed steel stud wall systems under fire conditions. Brisbane, Australia: Queensland University of Technology; 2010.
- [16] American Iron And Steel Institute. AISI S240–15, North American standard for cold-formed steel structural framing. USA: Washington D.C; 2015.
- [17] Schafer BW. Distortional buckling of cold-formed steel columns, American Iron and Steel Institute, 2000.
- [18] Schafer BW. Review: The Direct Strength Method of cold-formed steel member design. *J Constr Steel Res* 2008;64(7–8):766–78.
- [19] International Organization for Standardization. ISO 834–1 fire resistance tests - elements of buildings construction - Part-1 general requirements. Geneva: Switzerland; 1999.
- [20] Keerthan P, Mahendran M. Numerical studies of gypsum plasterboard panels under standard fire conditions. *Fire Saf J* 2012;53:105–19.
- [21] Keerthan P, Mahendran M. Thermal performance of composite panels under fire conditions using numerical studies: plasterboards, rockwool, glass fibre and cellulose insulations. *Fire Technol* 2012;49(2):329–56.
- [22] Rusthi M, Keerthan P, Mahendran M, Ariyanayagam AD. Investigating the fire performance of LSF wall systems using finite element analyses. *J Struct Fire Eng* 2017;8(4):354–76.
- [23] Kankanamge ND, Mahendran M. Mechanical properties of cold-formed steels at elevated temperatures. *Thin-Wall Struct* 2011;49(1):26–44.
- [24] Standards Australia, AS 1530.4 - Methods for fire tests on building materials, components and structures - Part 4: Fire-resistance test of elements of construction, Sydney, Australia, 2005.
- [25] Plasterboard Boral. Selector+ Plasterboard Systems Issue 2. Sydney, Australia: Boral Plasterboard Limited; 2009.